Nano Research
2022, 15(8): 6831–6840

ISSN 1998-0124 CN 11-5974/O4
https://doi.org/10.1007/s12274-022-4511-3

Research Article

Hollow hydrangea-like nitrogen-doped NiO/Ni/carbon composites as lightweight and highly efficient electromagnetic wave absorbers

Jin Liang[1], Chunwei Li[1], Xin Cao[1], Yuxiang Wang[1], Zongcheng Li[1], Benzheng Gao[2], Zeyou Tong[2], Bin Wang[3] (✉), Shuchen Wan[2], and Jie Kong[1] (✉)

[1] *MOE Key Laboratory of Materials Physics and Chemistry in Extraordinary Conditions, Shaanxi Key Laboratory of Macromolecular Science and Technology, School of Chemistry and Chemical Engineering, Northwestern Polytechnical University, Xi'an 710072, China*
[2] *China Academy of Launch Vehicle Technology, Beijing 100076, China*
[3] *Minmetals exploration & development CO. LTD, Beijing 100010, China*

Received: 12 April 2022 / **Revised:** 6 May 2022 / **Accepted:** 7 May 2022

ABSTRACT

Hierarchical hollow-structured magnetic–dielectric materials are considered to be promising and competitive functional absorbers for microwave absorption (MA). Herein, a hierarchical hollow hydrangea multicomponent metal oxides/metal-carbon was designed and successfully produced via a facile self-assembly method and calcination process. Adequate magnetic NiO and Ni nanoparticles were suspended within the hollow hydrangea-like nitrogen-doped carbon matrix (HH N-NiO/Ni/C), constructing a unique hierarchical hollow structured multicomponent magnetic–dielectric MA composite. The annealing temperature and oxidation time were carefully regulated to investigate the complex permittivity and permeability. HH N-NiO/Ni/C delivers exceptional MA properties with maximum reflection loss of –45.8 dB at 1.7 mm thickness and displays a wide effective absorption frequency range of 5.6 GHz. The superior MA performance can be attributed to the following aspects: (1) The hierarchical hollow multicomponent structure offers plentiful of heterojunction interfaces triggering interfacial polarization; (2) nitrogen doped-carbon (N-C) facilitates the conductive loss by the unique electron migration path in the graphitized C and NiO/Ni; (3) magnetic NiO/Ni nanoparticles homogeneously dispersed within N-C form extensive C skeleton and strengthen the magnetic response ability; (4) hierarchical hollow wrinkled structures possess a large interspace and heterogeneous interface improving polarization loss and enhancing multireflection process and the unique structure satisfies magnetic and dielectric loss simultaneously resulting from synergistic effects of different components within the composites.

KEYWORDS

hierarchical magnetic–dielectric composites, hollow hydrangea-like structure, impedance matching, nitrogen doped NiO/Ni/C, microwave absorption

1 Introduction

With the fifth-generation wireless systems and the use of multiband radar in military equipment, microwave absorption (MA) materials with high-efficiency and broadband are urgently required to address the severe electromagnetic radiation pollution caused by the diverse electronic products [1–3]. MA materials can be separated into three categories according to the main loss mechanism, dielectric loss, magnetic loss, and conductivity loss materials. However, nor of them comfort to the science and technology development to absorbers' requirement of thin, light, broadband, and strong. High-efficient MA materials demand to simultaneously generate the strong magnetic loss and dielectric dissipation.

Dielectric loss materials (semiconductor metal oxide and ferroelectric ceramics) possess low density, high aspect ratio, and good antioxidation capability benefiting the "light" character for ideal microwave absorbers. However, this kind absorber with high conductivity easily led to benign impedance mismatching [4–7]. Magnetic loss materials (ferrite and fine metal powder, etc.) have perfect magnetic loss ability. However, the high density of this kind absorber is inconsistent with the "lighter weight and thin layer" demand, hindering practical applications [8–12]. Conductive loss materials often have high conductivity and strong reflection of the incident electromagnetic wave. So, high conductivity carbon materials such as graphene and carbon nanotubes are often used in the field of electromagnetic shielding [13–16]. Each type of materials possesses their superiority, but they cannot construct the balanced electromagnetic property in absorbers for the single electromagnetic loss mechanism [17]. Therefore, magnetic–dielectric composites with controllable electric/magnetic components and synergy loss mechanism become a research hotspot.

Magnetic–dielectric composites are considered as competitive and promising microwave absorbing materials by the functional expression toward advanced materials. In view of the importance of magnetic–dielectric composites in enhancing the MA property, many studies of magnetic–dielectric-based absorbers have been explored. Che's group successfully prepared Co@NC–ZnO absorbers with electron conduction and magnetic coupling

Address correspondence to Bin Wang, wangbin0502@163.com; Jie Kong, kongjie@nwpu.edu.cn

network achieving a confined electromagnetic (EM) balance [18]. Lu's group synthesized sandwich-like Fe&TiO_2@C composites from MXene–metal-organic frame hybrids as the MA materials. The existence of Fe and TiO_2 anchored in carbon nanosheets offered good impedance matching and strong reflection loss (–51.8 dB at 6.6 GHz) [19]. Many heterogeneous components provide numerous interfaces that permit the accumulation of electrons and promote electromagnetic energy attenuation. Our group prepared unique hollow bowl-like nitrogen-doped Co/C (HBN-Co/C) using a facile two-step method. Compared with former studies, HBN-Co/C composites displayed a perfect absorption performance with the minimum reflection loss of –42.3 dB at 13.3 GHz with a thickness of 1.9 mm and wide bandwidth (12.9–18.0 GHz). The excellent electromagnetic absorption performance is primarily attributed to the synergistic effects among the multiple components, interface polarization loss, dielectric loss, and magnetic loss [20]. In short, the construction and synergy loss mechanism of magnetic–dielectric composites have become research hotspots. However, it is still an enormous challenge to simultaneously adjust dielectric and magnetic property parameters of magnetic–dielectric composite absorbers at the nano-scale.

In this work, hierarchical hollow hydrangea-like N-doped NiO/Ni/C nanosheet spheres (HH N-NiO/Ni/C) were first successfully formed via a facile self-assembly method and calcination process as MA materials. Magnetic NiO and Ni nanoparticles suspended within hollow hydrangea-like N-doped C (N-C) matrix, constructing multidimensional magnetic coupling network and strengthening the magnetic dissipation capability. The generated heterojunction interfaces among NiO, Ni, and C trigger interfacial polarization, boosting the dielectric loss. The proper sizes and dispersion states of NiO and Ni had an important influence on the effective permittivity and electromagnetic wave absorption. The defects induced by heteroatoms, produce the outstanding electron migration/hop paths to optimize the permittivity, conduction loss, and impedance matching of the composites. All the above superiorities can synergistically regulate the parameters of dielectric and magnetic properties. In addition, these hollow structures are beneficial to increased reflection loss and broader absorption band as well as the "low-weight" character. In particularly, these hierarchical two-dimensional (2D) nanosheets assembled form multi-component hollow hydrangea composites exhibit excellent MA performance.

2 Experiments section

2.1 Materials

All agents were applied defectively without any further purification. The $Co(NO_3)_2{\cdot}6H_2O$ (99%) was purchased from ACROS Organics USA. Hexamethylenetetramine (HMTA, $C_6H_{12}N_4$) and glucose ($C_6H_{12}O_6$) were purchased from Shanghai hutryan Co., Ltd, China.

2.2 Synthesis

2.2.1 Synthesis of hierarchical HH precursors

In the typical synthesis process, 5 mmol of nickel sulfate hexahydrate ($NiSO_4{\cdot}6H_2O$), 4 mmol of glucose, and 5 mmol of HMTA were added into 40 mL of deionized (DI) water and obtained the pellucidly green solution by ultrasonic dispersion for 30 min. Then, the upper solution was transferred in the Teflon-lined stainless-steel autoclave and heated to 180 °C for 24 h. After cooling down to room temperature, the HH precursors were collected by centrifugation rinsing thoroughly with DI water and ethanol. The solid powder was hierarchical HH precursor.

2.2.2 Synthesis of hierarchical hollow hydrangea-like N-doped Ni/C (HH N-Ni/C) composites

The brown HH precursors were further calcined at 700, 800 and 900 °C for 3 h under N_2 with a heating rate of 5 °C/min. And HH N-Ni/C composites could be achieved. According to the calcination temperatures, the obtained production can be marked as HH N-Ni/C 700, HH N-Ni/C 800, and HH N-Ni/C 900.

2.2.3 Synthesis of hierarchical hollow hydrangea-like N-doped NiO/Ni/C (HH N-NiO/Ni/C) nanosheet spheres

HH N-Ni/C 700, HH N-Ni/C 800, and HH N-Ni/C 900 were calcined for different time (5, 10, and 20 min) under air at 300 °C with a heating rate of 1 °C/min, and HH N-NiO/Ni/C 700–5/10/20, HH N-NiO/Ni/C 800–5/10/20, and HH N-NiO/Ni/C 900–5/10/20 were finally achieved.

2.3 Characterization

The morphologies of the obtained materials were measured by field-emission scanning electron microscopy (FESEM, Verios G4, FEI, USA) with energy disperse spectroscopy (EDS) and transmission electron microscopy (TEM, Talos F200X, Thermo Fisher Scitific, USA). The weight loss of the composites was tested by thermogravimetric (TG, STA 449 F3, NETZSCH, Germany) analysis under N_2 atmospheres. The elements state of the materials was charactered by X-ray photoelectron spectroscopy (XPS, Axis Ultra DLD, UK) with a model Kratos Axis Ultra DLD (Al Kα radiation was generated at 15 kV and 150 W, C 1s 285 eV). Fourier transform-infrared (FT-IR) spectroscopy was applied to examine the state of amorphous carbon by Bruker Tensor 27. Crystal structure and constitution of the composites were measured by X-ray diffraction (XRD, Rigaku Mini Flex 600, Japan) using Cu Kα X-ray. Raman spectra were performed on the Alpha 300R (WI Tec, Germany) spectrometer. The N_2 adsorption–desorption isotherms were characterized according to the Brunauer–Emmett–Teller (BET) method (Bei Shi De 3H–2000 PS2, Beijing, China). The static magnetic properties were analyzed by multifunctional physical property measurement system (PPMS, Cryogenic CFMS–14T). Multifunctional physical property measurement system was employed to explore the influence of magnetic loss on MA wave attenuation.

3 Results and discussion

3.1 Synthesis and morphology of hollow hydrangea-like materials

The over overall synthesis is schematically illustrated in Fig. 1, taken HH N-doped NiO/Ni/C as example. The key step of preparing HH N-doped NiO/Ni/C is to synthesis HH precursors (Fig. S1(a) in the Electronic Supplementary Material (ESM)) by one-pot self-template method. The formation of the hollow structure can be explained as follows. At first, the prototype of the target product is smooth solid spheres which are formed via the heterogeneous nucleation process at the preliminary stage of the solvothermal reaction. Following with the reaction proceeded, the smooth spheres gradually roughen, because certain small and thin nanosheets anchor on the out surface of the solid spheres. Further prolongation of the reaction time results in partial cavitation of the pristine solid spheres, accompanied by an increase in the thickness and size of the nanoflakes on the surface. After reaction for 24 h, the pristine smooth solid spheres translate into HH precursors constructed by nanoflakes. The achieved materials display a spherical shape composed of interpenetrating network architecture nanosheets (Fig. S1(b) in the ESM) and the diameter is about 1,000 nm. The HH precursors possess a hollow structure,

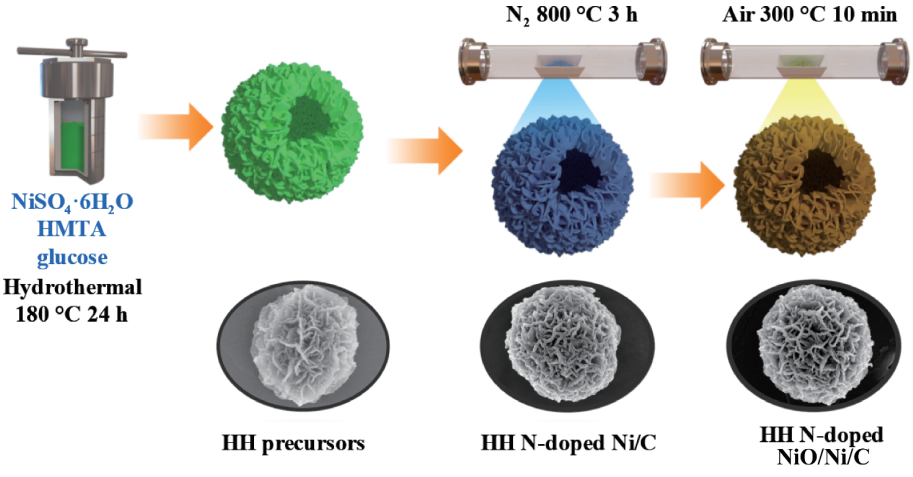

Figure 1 Schematic illustration of the fabrication procedure of HH N-doped NiO/Ni/C composites.

such as the hemisphere (Fig. S1(c) in the ESM) and broken materials (Fig. S1(d) in the ESM), these pristine structures are beneficial to harvest special architecture for multiple reflections and loss absorption of electromagnetic waves [21, 22]. From the enlarged scanning electron microscope (SEM) image, it can be seen that the thickness of the nanosheets (Fig. S1(e) in the ESM) are about 20 nm. Furthermore, the TEM image (Fig. S1(f) in the ESM) demonstrates that these interleaved nanosheets are thin and short, offering special electron conduction paths. After the second synthetic procedure, HH precursors were transferred into HH N-Ni/C composites under different pyrolysis conditions (700, 800, and 900 °C) and named as HH N-Ni/C 700, HH N-Ni/C 800, and HH N-Ni/C 900, respectively.

The morphologies of these materials were determined and shown in Fig. 2. These morphologies of three types have almost no discernible changes compared with the HH precursors, manifesting the excellent structural stability of HH N-Ni/C composites. For the enlarged images (Figs. 2(c), 2(f), and 2(j)) of the HH N-Ni/C nanosheets, the surfaces of HH N-Ni/C 800 and HH N-Ni/C 900 possess an apparent granular character compared with HH N-Ni/C 700. To our knowledge, these types of concave–convex cover can strengthen the scattering of electromagnetic waves to enhance electromagnetic absorption [23]. HH N-Ni/C 800 was further characterized in Fig. S3 in the ESM. For the TEM images (Figs. S3(a) and S3(b) in the ESM), it can be seen that the HH N-Ni/C 800 is essential to the nature of nanosheets and almost maintains the same diameter as the HH precursors. The higher-magnification TEM image (Fig. S3(c) in the ESM) shows that many nanoparticles anchor in the C layer and their size is about 7 nm (Fig. S3(d) in the ESM). The high-resolution TEM (HRTEM) image shows the well-defined interplanar distance of 0.245 nm (Fig. S3(e) in the ESM), which can be indexed to (111) crystal planes of metallic Ni. Moreover, the corresponding selected area electron diffraction (SAED) pattern of individual anchored nanoparticles (Fig. S3(f) in the ESM) shows two obvious rings, revealing the feature of metallic nickel and demonstrating the successful preparation of the designed magnetic–dielectric composites. It is well known that multiple components usually exhibit a wider spectrum range of MA along with stronger reflection loss. Based on this face, all the harvested composites were further exposed to oxidization in an air atmosphere. The three types of HH N-Ni/C were annealed in a tube furnace at 300 °C for 5, 10, and 20 min. After this procedure, the annealed materials well maintained the same structure of HH

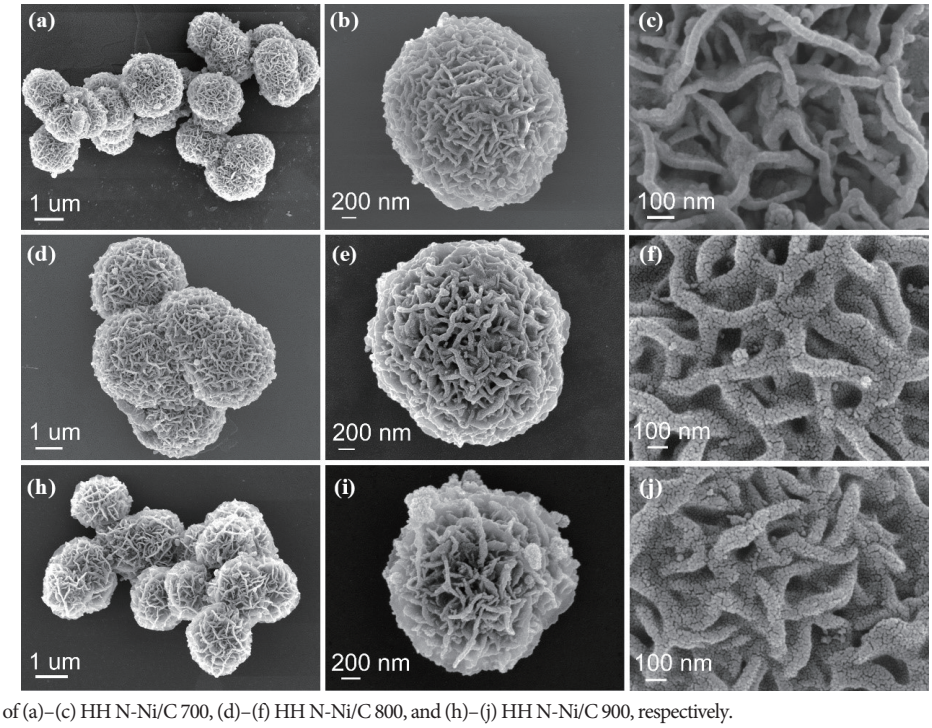

Figure 2 SEM images of (a)–(c) HH N-Ni/C 700, (d)–(f) HH N-Ni/C 800, and (h)–(j) HH N-Ni/C 900, respectively.

N-Ni/C, displaying excellent structural stability (Fig. S2 in the ESM). The morphology and distribution of elements of oxidized materials were subsequently analyzed in detail. HH N-NiO/Ni/C 800–10, for instance, is shown in Fig. 3. TEM images (Figs. 3(a) and 3(b)) reveal that the HH N-NiO/Ni/C 800–10 possesses the representative feature of a hollow porous structure and the thickness of the nanosheets is about 20 nm (Fig. 3(c)). Because of the loose and porous surface, part of the electromagnetic wave can enter the cavity of the absorber, which is conducive to the attenuation of electromagnetic waves. From the enlarged TEM image, the nanoparticles (Fig. 3(d)) enshrouded by a C layer still exist and the interplanar spacing is 0.238 nm which is confirmed as (200) crystal plane of Ni (Fig. 3(e)). The two SAED diffraction rings can be fitted to the (200) crystal plane of Ni and (220) crystal plane of NiO (Fig. 3(f)), proving the existence of Ni in the form of NiO and Ni [24].

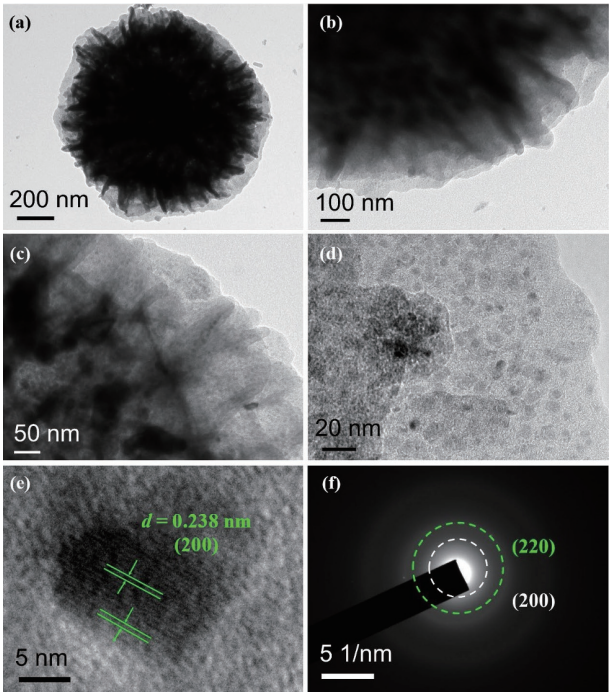

Figure 3 (a)–(d) TEM images, (e) HRTEM image, and (f) SAED pattern of HH N-NiO/Ni/C 800–10.

To demonstrate the distribution of elements of the HH N-NiO/Ni/C 800–10, EDS elemental mapping was employed on a representative hollow structure particle (Fig. 4(a)). The result (Figs. 4(b)–4(f)) illustrates the uniform distribution of Ni, C, and O, while less N existed distributed in the inner portion. EDS mapping images of HH N-NiO/Ni/C 800–0 (HH N-NiO/C 800), HH N-NiO/Ni/C 800–5, and HH N-NiO/Ni/C 800–20 are shown in Figs. S4–S6 in the ESM. Following the increase in oxidation time, NiO is slowly generated, and the amount increases. At the same time, the amounts of Ni, N, and O decrease along with pyrolysis temperatures (Table S1 in the ESM). Conversely, the content of C increases. To a certain degree, the composition of the MA materials is successfully adjusted using the postprocessing temperature. The controllability of HH N-NiO/Ni/C components is beneficial to balance dielectric–magnetic properties and impedance matching. In a word, these unique structures could promote multireflection, prolong the microwave transition paths, and enhance the microwave loss probability.

3.2 Phase composition and microstructure of the hollow hydrangea-like materials

The crystal structure of the obtained materials was confirmed by XRD result as shown in Fig. 5(a), the two peaks at 44.4° and 51.8° can be assigned to the planes (111) and (200) of metallic Ni (JCPDS 70-1849) [25, 26]. For the three oxidated samples, peaks at 2θ = 44.4°, 51.8°, and 76.35° can be attributed to the planes (111), (200), and (220) of Ni (JCPDS 70-1849), whereas the reflections corresponding to the planes (111) and (200) of NiO can be observed at 2θ = 37.1° and 43.3° (JCPDS 89-7130) for the oxidated composites. No obvious peaks of C have been detected corresponding to C in the three HH N-NiO/Ni/C samples, which are amorphous [27]. To verify this conclusion, Raman spectra were employed to measure the nature of carbon in the composites. As shown in Fig. 5(b), D and G bands appear at 1,360 and 1,573 cm^{-1}, illustrating the existence of amorphous carbon [28]. The ratio I_D/I_G can be applied to calculate the degree of carbon disorder. The ratios of the three samples are 2.79, 2.36, and 1.52, respectively. A high value of the ratio means more graphitic structure, fewer defects, and better electrical conductivity [29]. The increase of ordered phase content can not only increase the ordered/disordered phase interface, but also tends to have more defects and impurities distributed at the interface. This could

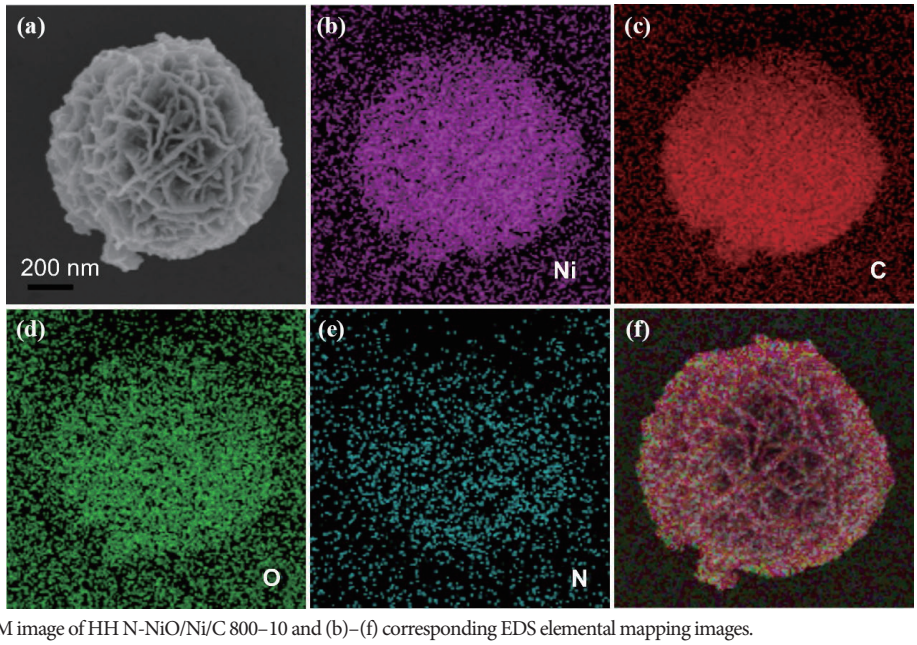

Figure 4 (a) Typical SEM image of HH N-NiO/Ni/C 800–10 and (b)–(f) corresponding EDS elemental mapping images.

provide more multiploidization centers for the material polarization relaxation, further increasing the electromagnetic parameters of the composite absorbers, and effectively improving the energy storage and loss capacity of the absorbers [30].

Specific surface area (SSA) and pore size distribution of the three samples were determined using BET method. As shown in Fig. 5(c), the N_2 adsorption/desorption isotherms of the N-NiO/Ni/C 700–10, N–NiO/Ni/C 800–10, and N–NiO/Ni/C 900–10 can be assigned to H3 of a type-IV hysteresis loop, demonstrating that the composites have micropores [31]. The SSAs of the three samples are 163.27, 167.05, and 252.54 m^2/g, respectively. It can be seen that the SSA of the observed absorbers increases with the increase of annealing temperature, which can be attributed to the escape of unstable structures during pyrolysis. Figure 5(d) demonstrates that the pore sizes of the three composites concentrated at ~ 4 nm. Nonlamellar absorber microspheres have high SSAs, and wedge-shaped pores provide favorable conditions for electromagnetic absorption. At the same time, the pores also form abundant lamellar/lamellar and microsphere/air interfaces, which provide favorable conditions for relaxation loss [32].

XPS measurement was introduced to characterize the elemental valence and chemical composition of the obtained materials. As displayed in Fig. 6(a), the survey spectrum illustrates that the existence of C, N, O, and Ni in the N-NiO/Ni/C 800–10. In the high-resolution XPS spectra of Ni 2p for HH N-NiO/Ni/C 800–10 (Fig. 6(e)), the peaks at 854.2, 855.8, and 872.1 eV can be ascribed to Ni $2p_{2/3}$ and Ni $2p_{1/2}$ of NiO, and the corresponding satellite peaks are situated at 858.8 and 874.4 eV, respectively. Two peaks at 853.5 and 870.2 eV can be assigned to Ni, and the corresponding satellite peaks appear at 858.8 and 874.4 eV, according with the XRD results. The high-resolution N 1s spectra (Fig. 6(d)) of HH N-NiO/Ni/C 800–10 can be fitted to pyridine N, pyrrole N, and graphite N at 398.5, 399.5, and 401.0 eV, respectively. Pyridine N and pyrrole N could offer extra polarization for electromagnetic MA and graphite N promotes the conductivity of the carbon skeleton [31]. For C 1s spectra (Fig. 6(c)), peaks at 284.6, 285.5, 286.7, and 288.8 eV are related to C–O, C–N, O–C=O, and C–C bonds, respectively. C–N bonds can mainly increase the conductivity and dielectric polarization of the absorbers [33]. The O 1s spectra (Fig. 6(b)) demonstrate that these composites possess adequate functional groups including C–O, O–C=O, and Ni–O at 529.4, 532.4, and 533.9 eV, respectively. The content of every element was calculated using Casa XPS software as shown in Table S1 in the ESM, which is in keeping with the mapping results. All of these evidences prove that the structures possess asymmetric charge density differences, demonstrating the formation of dipoles. From the previous researches, the dipoles can break loose, orient, and convert electromagnetic energy into heat energy by relaxation.

For the existence of NiO and Ni, a multifunctional physical property measurement system was employed to explore the influence of magnetic loss on MA wave attenuation. As shown in Fig. S7 in the ESM, the three samples exhibit S-type hysteresis loops revealing the characteristics of soft magnetic materials. The coercivity (H_c) values of the three samples are 108, 186, and 192 Oe. As reported, the value of H_c is relative to the size of the absorber's particles [34]. That value is increasing meaning that the size of the nanoparticles grows following the increase in the annealing temperature. Magnetization can be regarded as the vector sum of the dipole magnetic moments of the material. The saturation magnetizations (M_s) of the three samples are 4.2, 5.9, and 12.3 emu/g. For the hollow-structured materials, the hollow inner concaves are produced as a nonferromagnetic medium. The increasing M_s from HH N-NiO/Ni/C 700–10 to HH N-NiO/Ni/C 900–10 shows that a high magnetic–dielectric is beneficial to the crystallinity of the NiO/Ni nanoparticles and suppresses surface effects improving the magnetic particles' degree of order.

3.3 EM wave absorption performance

The electromagnetic MA performance was characterized by reflection loss (RL) as precious research reported [35, 36]. The electromagnetic properties of absorbers are determined by the complex permittivity ($\varepsilon_r = \varepsilon' - j\varepsilon''$) and permeability ($\mu_r = \mu' - j\mu''$) primarily, where ε' is permittivity, ε'' is imaginary permittivity, μ' is real permeability, and μ'' is imaginary permeability. As displayed in Fig. 7(a), the ε' of the HH N-NiO/Ni/C 700–10, HH N-NiO/Ni/C 800–10, and HH N-NiO/Ni/C 900–10 delivers a gently decreasing tendency from 6.4 to 4.9, 12 to 5.4, and 18.1 to 8.4, respectively, with increasing frequency. This phenomenon is

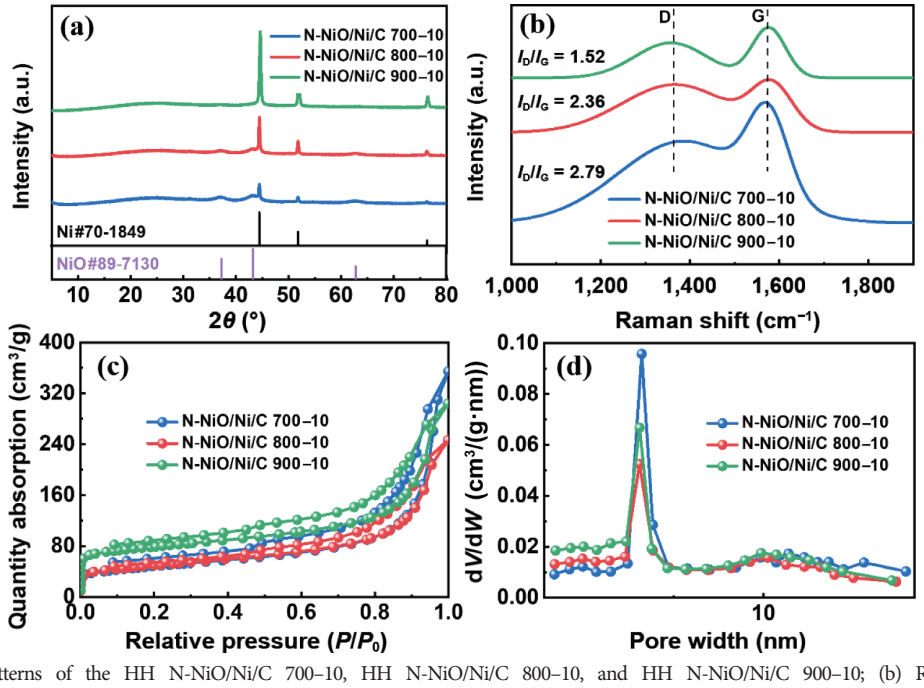

Figure 5 (a) XRD patterns of the HH N-NiO/Ni/C 700–10, HH N-NiO/Ni/C 800–10, and HH N-NiO/Ni/C 900–10; (b) Raman spectra, (c) N_2 adsorption–desorption curves, and (d) pore size distribution of HH N-NiO/Ni/C 700–10, HH N-NiO/Ni/C 800–10, and HH N-NiO/Ni/C 900–10, respectively.

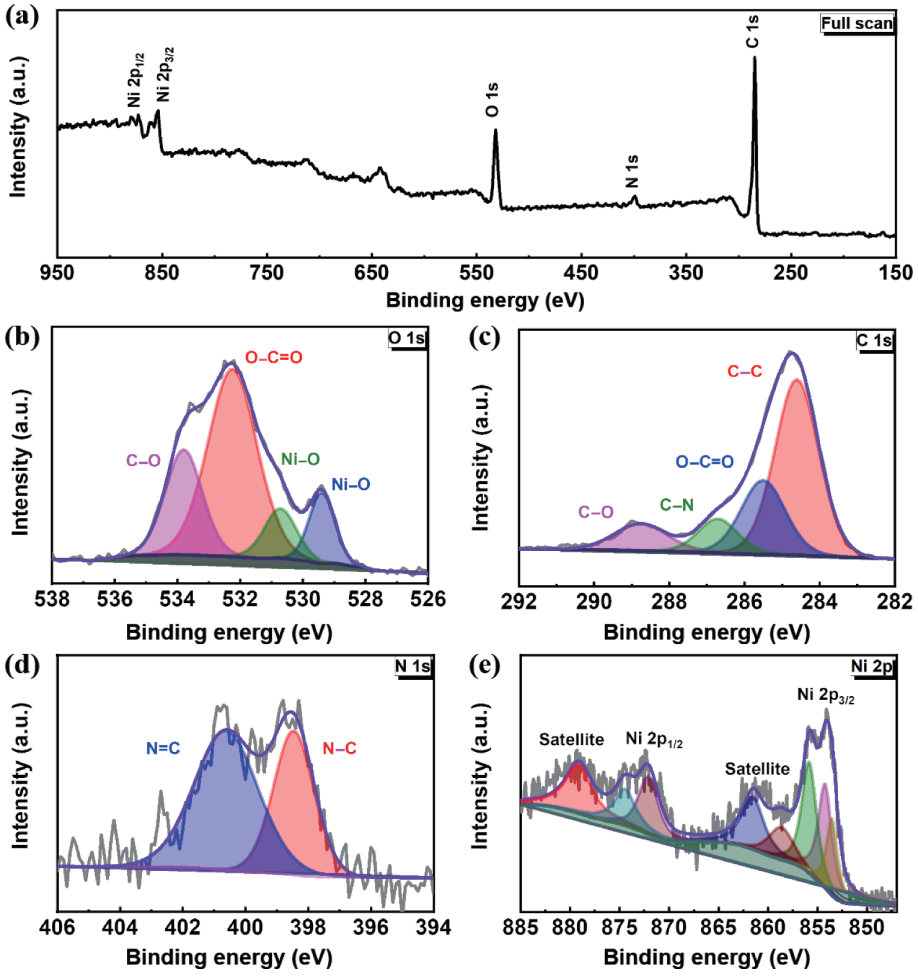

Figure 6 XPS spectra of HH N-NiO/Ni/C 800–10: (a) full scan, (b) C 1s, (c) O1s, (d) N 1s, and (e) Ni 2p spectra.

caused by the reciprocating frequency of the dipole reaching the limit, which cannot synchronize with the electromagnetic wave frequency, resulting in hysteresis and the gradually decreased ε' [37]. With the increase of pyrolysis temperature, the ε' of the different samples increases. The higher the pyrolysis temperature is, the more ordered carbon phase becomes and the more polarization centers are formed. The increase of polarization centers enhances the material's energy storage ability, so the ε' increases following the pyrolysis temperature [38]. Resonance peaks caused by the polarization relaxation phenomenon are observed at 12.0, 14.5, and 16.8 GHz, showing that many polarization relaxation mechanisms exist in the absorbers [39]. The ε'' of all the composites are shown in Fig. 7(b), and the variation of the ε'' is similar to that of ε'. The ε'' values of the three composites also express a decreasing tendency between 2 and 18 GHz from 1.6 to 1.2, 6.5 to 4.2, and 16 to 5.0. This positive phenomenon can be clearly observed in Raman spectra. With the increase of pyrolysis temperature, the C content of graphite in carbon skeleton increases to generate more multiploidization units, resulting in more multiploidization relaxation. Therefore, the ε'' representing dielectric loss capacity also increases with the increase of ordered phase content [40]. The tangent value of the dielectric loss ($\tan\delta_\varepsilon$) always signifies the conductivity loss ability as shown in Fig. 7(c). $\tan\delta_\varepsilon$ increases with pyrolysis temperature, although both ε' and ε'' increase with pyrolysis temperature, because the increase of ε' is smaller than that of ε''. The three samples' $\tan\delta_\varepsilon$ displays a little change between 2 and 18 GHz (0.16–0.36, 0.45–0.67, and 0.51–0.88), indicating the low dielectric loss ability in the frequency window. $\tan\delta_\varepsilon$ of HH N-NiO/Ni/C 900–10 possesses the highest value, meaning that this sample has the strongest loss of electromagnetic waves entering the material. The much higher $\tan\delta_\varepsilon$ may lead to impedance imbalance, so the proper $\tan\delta_\varepsilon$ can be one of the important factors in evaluating the properties of absorbers. For further comparision, electromagnetic parameters of samples (HH N–NiO/Ni/C 700, HH N–NiO/Ni/C 800, and HH N–NiO/Ni/C 900) oxided with different time were also tested and displayed in Figs. S9–S12 in the ESM.

Cole–cole plots describe the relationship of ε' and ε'' by Debye relaxation theory [41]. To further explore the dielectric loss process of the HH N-NiO/Ni/C samples, Cole–cole (ε'–ε'') plots are adopted to analyze the polarization loss mechanism. The Cole–cole plots of the three samples are shown in Fig. S13(a) in the ESM. Among the three samples, there is no straight line in the Cole–cole semicircle of the HH N-NiO/Ni/C 700–10 sample (Fig. S13(b) in the ESM), indicating that the sample has poor conductivity. The Cole–cole semicircles produced by HH N-NiO/Ni/C 800–10 (Fig. S13(c) in the ESM) and HH N-NiO/Ni/C 900–10 (Fig. S13(d) in the ESM) has long straight lines. Here, the HH N–NiO/Ni/C 900–10 straight line is the longest, indicating that the growing pyrolysis temperature leads to the increase in the conductivity and conductance loss of the absorbers. In addition, the Cole–cole semicircle of the three samples is not smooth, which is mainly caused by the effects of various interface polarization mechanisms, such as carbon skeleton defects, defects originating from O and N atoms, and the high SSA of the material itself on the relaxation process. One semicircle of the Cole–cole plot expresses a type of polarization process. In the plot of N-NiO/Ni/C 800–10, multiple semicircles are discovered in the complex scatter plots, sustaining multiple polarization processes. The multiple polarization processes primarily appear on the outer

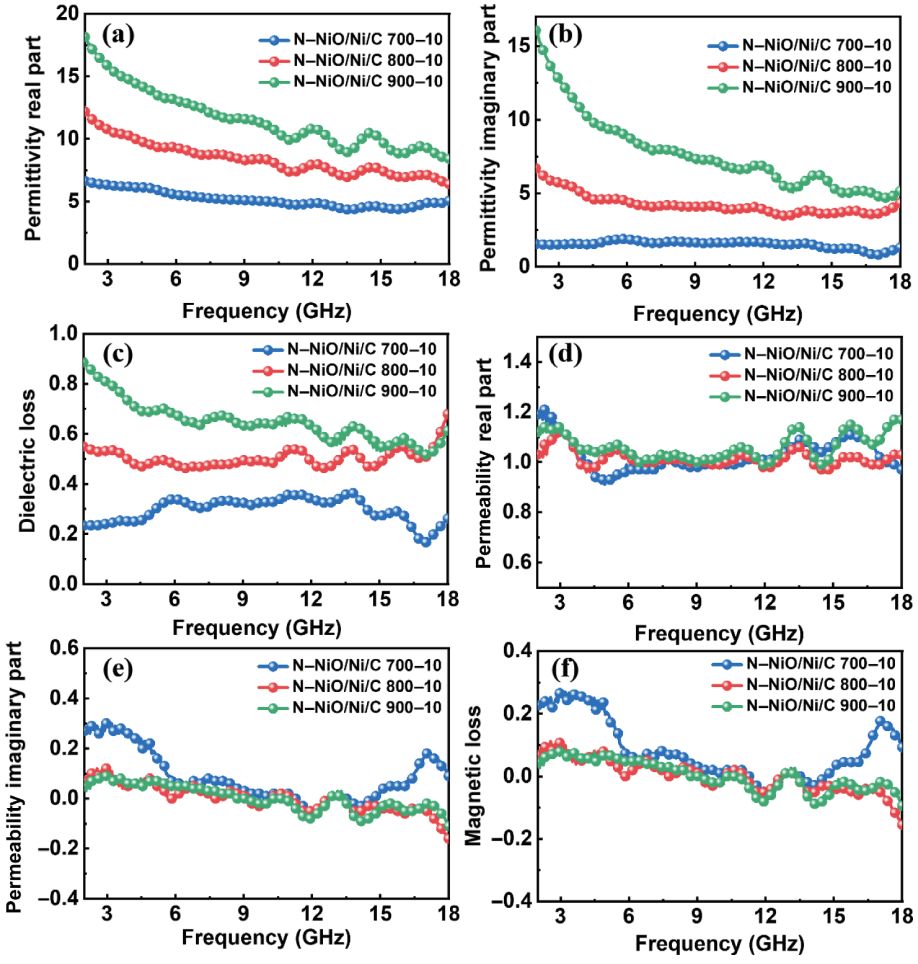

Figure 7 (a) Real permittivity ε', (b) imaginary permittivity ε'', (c) $\tan\delta_\varepsilon$, (d) real permeability μ', (e) imaginary permeability μ'', and (f) $\tan\delta_\mu$ of HH N-NiO/Ni/C 700–10, HH N-NiO/Ni/C 800–10, and HH N-NiO/Ni/C 900–10, respectively.

nanosheet of the hollow N-NiO/Ni/C 800–10 spheres when incident microwaves arrive at the nanosheet surface, because of the efficient separation of charge centers. Polarization processes can be greatly facilitated by multiple internal reflections in the inner cavity of the individual hollow hydrangeas and reflections among the hollow hydrangeas promote the contact frequency between electromagnetic waves and the outer nanosheet surfaces.

The complex permeability (real permeability μ' and imaginary permeability μ'') and tangent magnetic loss ($\tan\delta_\mu$) of the three samples are displayed in Figs. 7(d) and 7(e). The apparent resonance peaks can be detected in the plot of μ'' against frequency, revealing magnetic loss caused by the Ni/NiO. The results indicate the $\tan\delta_\varepsilon$ values of these three absorbers are greater than that of $\tan\delta_u$, and manifest dielectric loss as the primary loss mechanism in the MA process for the HH N-NiO/Ni/C/paraffin composites [41]. To our knowledge, that natural resonance always appears in the low-frequency region, whereas the exchange resonance may correspond to the high-frequency resonance peaks. Apart from this, eddy loss is also an important path for magnetic loss and can be expressed by the eddy current coefficient (C_0) ($C_0 = \frac{\mu''}{\mu'^2 f}$) [42]. From Fig. S14 in the ESM, C_0 of the three samples decreases between 2 to 6 GHz, and is maintained almost constant in the frequency range of 6–18 GHz, inferring that the eddy current loss contributed to microwave attenuation in the Ku-band.

To investigate the electromagnetic absorption performance of the achieved composite materials, RL, as an effective indicator for evaluating MA performance, was calculated by using the electromagnetic parameters according to transmission line theory. Figure 8 depicts the RL curves of different dimensions with a thickness from 1.0 to 4.0 mm in the measured frequency range (2–18 GHz). Figures 8(b), 8(e), and 8(h) shows the 2D, three-dimensional (3D), and contour maps of the RL values for NiO/Ni/C 800–10 composites. As shown in Figs. 8(b) and 8(e), the minimum RL (RL_{min}) of NiO/Ni/C 800–10 is –45.8 dB at 17.15 GHz with the thickness of 1.7 mm, and at the thickness of 1.9 mm, it reaches the max effective absorption bandwidth (EAB) reaching 5.6 GHz (from 12.4 to 18.0 GHz). According to the contour maps of NiO/Ni/C 800–10 (Fig. 8(h)), it can be found that the thickness is between 1.5–4.0 mm, and there is an effective absorption area, that is, the effective absorption of electromagnetic waves in 5.36–18 GHz can be achieved by adjusting the thickness of the sample. For NiO/Ni/C 700–10 (Figs. 8(a), 8(d), and 8(g)) and NiO/Ni/C 900–10 (Figs. 8(c), 8(f), and 8(i)), the RL_{min} and EAB are –15.25 dB (4.0 mm)/3.5 GHz (10.2–13.72 GHz) and –20.15 dB (1.5 mm)/5.28 GHz (12.72–18.0 GHz), respectively. Compared with NiO/Ni/C 700–10 and NiO/Ni/C 900–10, NiO/Ni/C 800–10 achieves the RL_{min} and the widest effective absorption band. This electromagnetic absorption ability is more favorable than that of most Ni-based nanocomplexes. Based on the thickness (mm) and RL_{min}, N-NiO/Ni/C 800–10 achieved a better electromagnetic absorption ability than all of the previous Ni–based microwave absorbers. A detailed comparison of these electromagnetic absorbing materials is displayed in Fig. 9 and Table S2 in the ESM [43–59].

To explore the reasons for the difference in absorbing performance among samples, the two parameters of the three samples' attenuation constant and impedance matching (Z_{in}) value are discussed. α represents whether the incident microwave

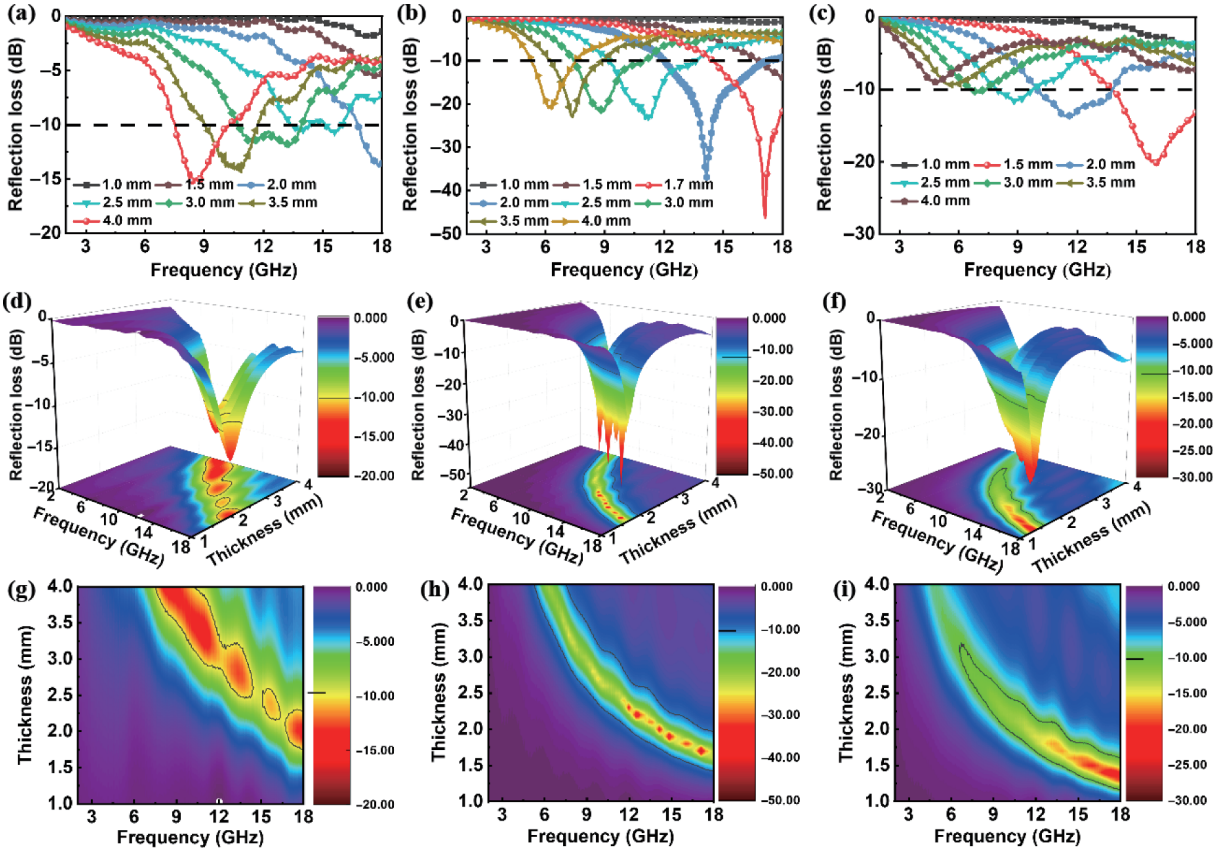

Figure 8 (a)–(c) 2D images, (d)–(f) 3D images, and (g)–(i) contour maps of calculated theoretical RL value of HH N-NiO/Ni/C 700–10, HH N-NiO/Ni/C 800–10, and HH N-NiO/Ni/C 900–10, respectively.

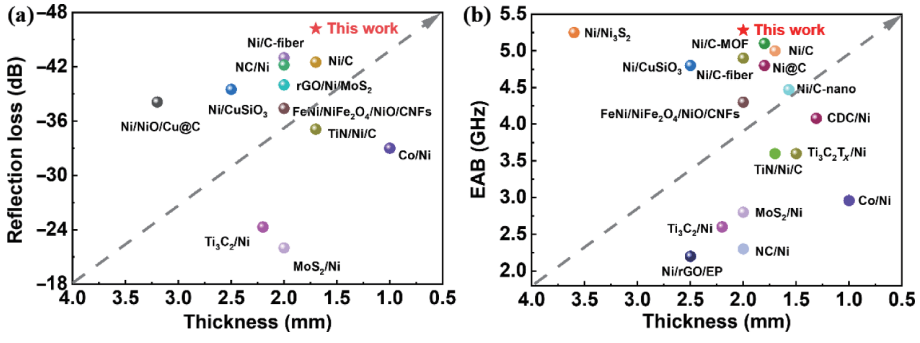

Figure 9 Comparison of microwave absorbing performance of Ni-based absorbers. (a) RL versus thickness and (b) RL versus EAB.

energy could be effectively attenuated. Z_{in} determines the transmission degree of the incident electromagnetic wave. The excellent impedance matching means that the great majority of the incident electromagnetic wave will transmit into the absorbers rather than reflect at the outer surface. Effective permittivity may be decreased by reducing the impedance gap between the absorbers via the architecture of the hollow structures with hierarchical, pore engineering, and synergistic effects between the magnetic and dielectric components. For the HH NiO/Ni/C composites, all the mentioned strategies are beneficial to impedance matching. As illustrated in Figs. S15(a) and S15(b) in the ESM, though the value of HH NiO/Ni/C 900–10 is higher than that of HH NiO/Ni/C 800–10, the Z_{in} value of HH NiO/Ni/C 800–10 is much closer to 1, displaying exceptional impedance matching and perfect attenuation ability. HH NiO/Ni/C 800–10 thus achieved both remarkable absorption ability and broad bandwidth.

Based on the above characterization and analysis, the electromagnetic wave (EMW) absorption mechanisms of the HH NiO/Ni/C 800–10 composites are displayed and declined in Fig. 10. First, the magnetic coupling network and conductivity network are compatible together in the HH NiO/Ni/C 800–10 hybrids constructed by the dispersed magnetic NiO/Ni nanoparticles within the N–C built with an extensive carbon skeleton; second, the hierarchical hollow multicomponent structure offers plentiful heterojunction interfaces and triggers interfacial polarization, including dipolar polarization, natural resonance, and eddy loss; third, hollow wrinkled structures possess large interspaces and heterogeneous interface improving polarization loss and enhancing multireflection and scattering processes; fourth, N-doped C facilitates the conductive loss by the unique electron migration path in the graphitized C and NiO/Ni. As-synthesized HH NiO/Ni/C 800–10 exhibits confined and balanced magnetic and dielectric loss, creating the widest absorption bandwidth of 5.6 GHz (Ku-band).

4 Conclusions

In summary, the uniform hierarchical hollow hydrangea-like NiO/Ni/C composites were successfully achieved via a facile

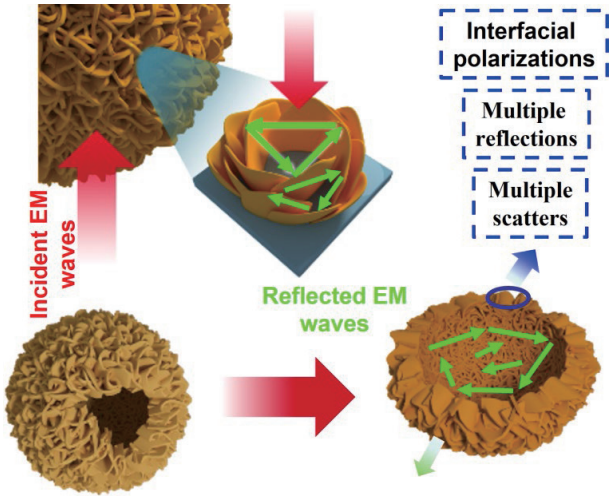

Figure 10 Possible microwave absorption mechanism of HH NiO/Ni/C 800–10.

strategy for EMW absorptions. The annealing temperature and oxidation time play important roles in the degree of crystallinity of C, composites' components, and EMW absorption. The magnetic coupling network and conductivity network of the hollow structure combined with the multiple components and structures endow the HH NiO/Ni/C 800–10 with matched impedance and good attenuation ability. Finally, it is hoped that this research will provide information for future explorations on the design of self-assembled hollow structures with advantageous EMW absorption properties.

Acknowledgements

This work was supported by the China Academy of Launch Vehicle Technology (Nos. 5120200522 and 5120210234), the National Natural Science Foundation of China (No. 21875190), Foundation of Aeronautics Science Fund (No. 2020Z056053002), and Fundamental Research Funds for the Central Universities (construction and low-frequency microwave absorption properties of metamaterials).

Electronic Supplementary Material: Supplementary material (electromagnetic paraments test, SEM and TEM images of HH precursors and HH N-NiO/Ni/C; elements' contents, hysteresis loop, and thermogravimetric curve of N-NiO/Ni/C700–10, N-NiO/Ni/C800–10, and N-NiO/Ni/C900–10; and supplementary electromagnetic performances) is available in the online version of this article at https://doi.org/10.1007/s12274-022-4511-3.

References

[1] Iqbal, A.; Shahzad, F.; Hantanasirisakul, K.; Kim, M. K.; Kwon, J.; Hong, J.; Kim, H.; Kim, D.; Gogotsi, Y.; Koo, C. M. Anomalous absorption of electromagnetic waves by 2D transition metal carbonitride Ti_3CNT_x (MXene). *Science* **2020**, *369*, 446–450.

[2] Qiao, J.; Zhang, X.; Liu, C.; Lyu, L. F.; Yang, Y. F.; Wang, Z.; Wu, L. L.; Liu, W.; Wang, F. L.; Liu, J. R. Non-magnetic bimetallic MOF-derived porous carbon-wrapped TiO_2/$ZrTiO_4$ composites for efficient electromagnetic wave absorption. *Nano-Micro Lett.* **2021**, *13*, 75.

[3] Lv, H. L.; Yang, Z. H.; Wang, P. L.; Ji, G. B.; Song, J. Z.; Zheng, L. R.; Zeng, H. B.; Xu, Z. J. A voltage-boosting strategy enabling a low-frequency, flexible electromagnetic wave absorption device. *Adv. Mater.* **2018**, *30*, 1706343.

[4] Huang, X. G.; Qiao, M.; Lu, X. C.; Li, Y. F.; Ma, Y. B.; Kang, B.; Quan, B.; Ji, G. B. Evolution of dielectric loss-dominated electromagnetic patterns in magnetic absorbers for enhanced microwave absorption performances. *Nano Res.* **2021**, *14*, 4006–4013.

[5] Gu, W. H.; Sheng, J. Q.; Huang, Q. Q.; Wang, G. H.; Chen, J. B.; Ji, G. B. Environmentally friendly and multifunctional shaddock peel-based carbon aerogel for thermal-insulation and microwave absorption. *Nano-Micro Lett.* **2021**, *13*, 102.

[6] Cheng, Y.; Seow, J. Z. Y.; Zhao, H. Q.; Xu, Z. J.; Ji, G. B. A flexible and lightweight biomass-reinforced microwave absorber. *Nano-Micro Lett.* **2020**, *12*, 125.

[7] Han, Y. X.; Ruan, K. P.; Gu, J. W. Janus (BNNS/ANF)-(AgNWs/ANF) thermal conductivity composite films with superior electromagnetic interference shielding and Joule heating performances. *Nano Res.* **2022**, *15*, 4747–4755.

[8] Xu, C. Y.; Wang, L.; Li, X.; Qian, X.; Wu, Z. C.; You, W. B.; Pei, K.; Qin, G.; Zeng, Q. W.; Yang, Z. Q. et al. Hierarchical magnetic network constructed by CoFe nanoparticles suspended within "tubes on rods" matrix toward enhanced microwave absorption. *Nano-Micro Lett.* **2021**, *13*, 47.

[9] Zhang, Y. L.; Ma, Z. L.; Ruan, K. P.; Gu, J. W. Multifunctional $Ti_3C_2T_x$-(Fe_3O_4/polyimide) composite films with Janus structure for outstanding electromagnetic interference shielding and superior visual thermal management. *Nano Res.* **2022**, *15*, 5601–5609.

[10] Yang, H. J.; Wang, X. P.; Wang, S. B.; Zhang, P. Y.; Xiao, C.; Sari, H. M. K.; Liu, J. H.; Jia, J. C.; Cao, B.; Qin, J. et al. Double boosting single atom Fe-N_4 sites for high efficiency O_2 and CO_2 electroreduction. *Carbon* **2021**, *182*, 109–116.

[11] Zhang, Y. L.; Gu, J. W. A perspective for developing polymer-based electromagnetic interference shielding composites. *Nano-Micro Lett.* **2022**, *14*, 89.

[12] Du, Y. Z.; Wang, X. D.; Dai, X. Y.; Li, W. X.; Tang, Y. S.; Kong, J. Ultraflexible, highly efficient electromagnetic interference shielding, and self-healable triboelectric nanogenerator based on $Ti_3C_2T_x$ MXene for self-powered wearable electronics. *J. Mater. Sci. Tech.* **2022**, *100*, 1–11.

[13] Song, Y.; Yin, F. X.; Zhang, C. W.; Guo, W. B.; Han, L. Y.; Yuan, Y. Three-dimensional ordered mesoporous carbon spheres modified with ultrafine zinc oxide nanoparticles for enhanced microwave absorption properties. *Nano-Micro Lett.* **2021**, *13*, 76.

[14] Liang, J.; Chen, J.; Shen, H. Q.; Hu, K. T.; Zhao, B. N.; Kong, J. Hollow porous bowl-like nitrogen-doped cobalt/carbon nanocomposites with enhanced electromagnetic wave absorption. *Chem. Mater.* **2021**, *33*, 1789–1798.

[15] Wang, J. Q.; Wu, F.; Cui, Y. H.; Zhang, A. B.; Zhang, Q. Y.; Zhang, B. L. Efficient synthesis of N-doped porous carbon nanoribbon composites with selective microwave absorption performance in common wavebands. *Carbon* **2021**, *175*, 164–175.

[16] Wang, L.; Ma, Z. L.; Zhang, Y. L.; Qiu, H.; Ruan, K. P.; Gu, J. W. Mechanically strong and folding-endurance $Ti_3C_2T_x$ MXene/PBO nanofiber films for efficient electromagnetic interference shielding and thermal management. *Carbon Energy* **2022**, *4*, 200–210.

[17] Wang, L.; Huang, M. Q.; Qian, X.; Liu, L. L.; You, W. B.; Zhang, J.; Wang, M.; Che, R. C. Confined magnetic–dielectric balance boosted electromagnetic wave absorption. *Small* **2021**, *17*, 2100970.

[18] Deng, B. W.; Xiang, Z.; Xiong, J.; Liu, Z. C.; Yu, L. Z.; Lu, W. Sandwich-like Fe&TiO_2@C nanocomposites derived from MXene/Fe-MOFs hybrids for electromagnetic absorption. *Nano-Micro Lett.* **2020**, *12*, 55.

[19] Che, R. C.; Peng, L. M.; Duan, X. F.; Chen, Q.; Liang, X. L. Microwave absorption enhancement and complex permittivity and permeability of Fe encapsulated within carbon nanotubes. *Adv. Mater.* **2004**, *16*, 401–405.

[20] Sun, H.; Che, R. C.; You, X.; Jiang, Y. S.; Yang, Z. B.; Deng, J.; Qiu, L. B.; Peng, H. S. Cross-stacking aligned carbon-nanotube films to tune microwave absorption frequencies and increase absorption intensities. *Adv. Mater.* **2014**, *26*, 8120–8125.

[21] Quan, B.; Gu, W. H.; Sheng, J. Q.; Lv, X. F.; Mao, Y. Y.; Liu, L.; Huang, X. G.; Tian, Z. J.; Ji, G. B. From intrinsic dielectric loss to geometry patterns: Dual-principles strategy for ultrabroad band microwave absorption. *Nano Res.* **2021**, *14*, 1495–1501.

[22] Liang, J.; Hu, H.; Park, H.; Xiao, C. H.; Ding, S. J.; Paik, U.; Lou, X. W. Construction of hybrid bowl-like structures by anchoring NiO nanosheets on flat carbon hollow particles with enhanced lithium storage properties. *Energy Environ. Sci.* **2015**, *8*, 1707–1711.

[23] Calles, J. A.; Carrero, A.; Vizcaíno, A. J.; Lindo, M. Effect of Ce and Zr addition to Ni/SiO_2 catalysts for hydrogen production through ethanol steam reforming. *Catalysts* **2015**, *5*, 58–76.
[24] Zou, X.; Sun, Q.; Zhang, Y. X.; Li, G. D.; Liu, Y. P.; Wu, Y. Y.; Yang, L.; Zou, X. X. Ultrafast surface modification of Ni_3S_2 nanosheet arrays with Ni-Mn bimetallic hydroxides for high-performance supercapacitors. *Sci. Rep.* **2018**, *8*, 4478.
[25] Qian, R. F.; Zong, H. X.; Schneider, J.; Zhou, G. D.; Zhao, T.; Li, Y. L.; Yang, J.; Bahnemann, D. W.; Pan, J. H. Charge carrier trapping, recombination and transfer during TiO_2 photocatalysis: An overview. *Catal. Today* **2019**, *335*, 78–90.
[26] Shu, J. C.; Huang, X. Y.; Cao, M. S. Assembling 3D flower-like Co_3O_4-MWCNT architecture for optimizing low-frequency microwave absorption. *Carbon* **2021**, *174*, 638–646.
[27] Zhang, Z. Z.; Jia, B. R.; Liu, L.; Zhao, Y. Z.; Wu, H. Y.; Qin, M. L.; Han, K.; Wang, W. A.; Xi, K.; Zhang, L. et al. Hollow multihole carbon bowls: A stress-release structure design for high-stability and high-volumetric-capacity potassium-ion batteries. *ACS Nano* **2019**, *13*, 11363–11371.
[28] Li, J. Y.; Li, X. H.; Zhao, P. H.; Lei, D. Y.; Li, W. L.; Bai, J. T.; Ren, Z. Y.; Xu, X. L. Searching for magnetism in pyrrolic N-doped graphene synthesized via hydrothermal reaction. *Carbon* **2015**, *84*, 460–468.
[29] Chen, Y.; Li, J. Z.; Li, T.; Zhang, L. K.; Meng, F. B. Recent advances in graphene-based films for electromagnetic interference shielding: Review and future prospects. *Carbon* **2021**, *180*, 163–184.
[30] Liu, J. W.; Che, R. C.; Chen, H. J.; Zhang, F.; Xia, F.; Wu, Q. S.; Wang, M. Microwave absorption enhancement of multifunctional composite microspheres with spinel Fe_3O_4 cores and anatase TiO_2 shells. *Small* **2012**, *8*, 1214–1221.
[31] Sheng, Z. H.; Shao, L.; Chen, J. J.; Bao, W. J.; Wang, F. B.; Xia, X. H. Catalyst-free synthesis of nitrogen-doped graphene via thermal annealing graphite oxide with melamine and its excellent electrocatalysis. *ACS Nano* **2011**, *5*, 4350–4358.
[32] Moitra, D.; Dhole, S.; Ghosh, B. K.; Chandel, M.; Jani, R. K.; Patra, M. K.; Vadera, S. R.; Ghosh, N. N. Synthesis and microwave absorption properties of $BiFeO_3$ nanowire-RGO nanocomposite and first-principles calculations for insight of electromagnetic properties and electronic structures. *J. Phys. Chem. C* **2017**, *121*, 21290–21304.
[33] Liu, P. B.; Gao, S.; Zhang, G. Z.; Huang, Y.; You, W. B.; Che, R. C. Hollow engineering to Co@N-doped carbon nanocages via synergistic protecting-etching strategy for ultrahigh microwave absorption. *Adv. Funct. Mater.* **2021**, *31*, 2102812.
[34] Cui, X. Q.; Liang, X. H.; Liu, W.; Gu, W. H.; Ji, G. B.; Du, Y. W. Stable microwave absorber derived from 1D customized heterogeneous structures of Fe_3N@C. *Chem. Eng. J.* **2020**, *381*, 122589.
[35] Lan, D.; Gao, Z. G.; Zhao, Z. H.; Wu, G. L.; Kou, K. C.; Wu, H. J. Double-shell hollow glass microspheres@Co_2SiO_4 for lightweight and efficient electromagnetic wave absorption. *Chem. Eng. J.* **2021**, *408*, 127313.
[36] Zhao, B.; Guo, X. Q.; Zhou, Y. Y.; Su, T. T.; Ma, C.; Zhang, R. Constructing hierarchical hollow CuS microspheres via a galvanic replacement reaction and their use as wide-band microwave absorbers. *Crystengcomm* **2017**, *19*, 2178–2186.
[37] Lv, J.; Liang, X. H.; Ji, G. B.; Quan, B.; Liu, W.; Du, Y. W. Structural and carbonized design of 1D FeNi/C nanofibers with conductive network to optimize electromagnetic parameters and absorption abilities. *ACS Sustainable Chem. Eng.* **2018**, *6*, 7239–7249.
[38] Qu, Y. P.; Du, Y.; Fan, G. H.; Xin, J. H.; Liu, Y.; Xie, P. T.; You, S. X.; Zhang, Z. D.; Sun, K.; Fan, R. H. Low-temperature sintering graphene/$CaCu_3Ti_4O_{12}$ nanocomposites with tunable negative permittivity. *J. Alloys Compd.* **2019**, *771*, 699–710.
[39] Wang, L. X.; Zhou, P. P.; Guo, Y.; Zhang, J.; Qiu, X.; Guan, Y. K.; Yu, M. X.; Zhu, H. L.; Zhang, Q. T. The effect of $ZnCl_2$ activation on microwave absorbing performance in walnut shell-derived nano-porous carbon. *RSC Adv.* **2019**, *9*, 9718–9728.
[40] Feng, J.; Pu, F. Z.; Li, Z. X.; Li, X. H.; Hu, X. Y.; Bai, J. T. Interfacial interactions and synergistic effect of CoNi nanocrystals and nitrogen-doped graphene in a composite microwave absorber. *Carbon* **2016**, *104*, 214–225.
[41] Liu, X. G.; Li, B.; Geng, D. Y.; Cui, W. B.; Yang, F.; Xie, Z. G.; Kang, D. J.; Zhang, Z. D. (Fe, Ni)/C nanocapsules for electromagnetic-wave-absorber in the whole Ku-band. *Carbon* **2009**, *47*, 470–474.
[42] Zhao, H. Q.; Cheng, Y.; Lv, H. L.; Ji, G. B.; Du, Y. W. A novel hierarchically porous magnetic carbon derived from biomass for strong lightweight microwave absorption. *Carbon* **2019**, *142*, 245–253.
[43] Ying, T. P.; Zhang, J.; Liu, X. G.; Yu, J. H.; Yu, J. Y.; Zhang, X. F. Corncob-derived hierarchical porous carbon/Ni composites for microwave absorbing application. *J. Alloys Compd.* **2020**, *849*, 156662.
[44] Ren, H. D.; Shu, X. F.; Liu, Z. Y.; Zhou, J.; Ma, J. L.; Liu, Y.; Kong, L. B.; Min, F. F.; Shi, X. C.; Han, J. J. et al. *In-situ* synthesis of layered porous coal-derived carbon/Ni magnetic composites with promising microwave absorption performance. J. Magn. *Magn. Mater.* **2020**, *513*, 167231.
[45] Li, W. X.; Guo, F.; Wei, X. Q.; Du, Y. E.; Chen, Y. Q. Preparation of Ni/C porous fibers derived from jute fibers for high-performance microwave absorption. *RSC Adv.* **2020**, *10*, 36644–36653.
[46] Uddin, W.; ur Rehman, S.; Aslam, M. A.; ur Rehman, S.; Wu, M. Z.; Zhu, M. Z. Enhanced microwave absorption from the magnetic–dielectric interface: A hybrid rGO@Ni-doped-MoS_2. *Mater. Res. Bull.* **2020**, *130*, 110943.
[47] Liu, Y.; Ji, C.; Su, X. L.; He, X. H.; Xu, J.; Li, Y. Y. Enhanced microwave absorption properties of flaky MoS_2 powders by decorating with Ni particles. *J. Magn. Magn. Mater.* **2020**, *511*, 166961.
[48] Fan, G. H.; Jiang, Y. L.; Hou, C. X.; Deng, X. R.; Liu, Z. X.; Zhang, L. J.; Zhang, Z. D.; Fan, R. H. Extremely facile and green synthesis of magnetic carbon composites drawn from natural bulrush for electromagnetic wave absorbing. *J. Alloys Compd.* **2020**, *835*, 155345.
[49] Wang, Z. X.; Yu, Q.; Nie, W. C.; Chen, P. Preparation and microwave absorption properties of Ni/rGO/EP composite foam. *J. Mater. Res.* **2020**, *35*, 2106–2114.
[50] Shen, Y. Q.; Wei, Y. P.; Ma, J. Q.; Zhang, Y. C.; Ji, B. H.; Tang, J.; Zhang, L. Y.; Yan, P. Z.; Du, X. Y. Self-cleaning functionalized FeNi/$NiFe_2O_4$/NiO/C nanofibers with enhanced microwave absorption performance. *Ceram. Int.* **2020**, *46*, 13397–13406.
[51] Liu, Y.; Zhang, S.; Su, X. L.; Xu, J.; Li, Y. Y. Enhanced microwave absorption properties of Ti_3C_2 MXene powders decorated with Ni particles. *J. Mater. Sci.* **2020**, *55*, 10339–10350.
[52] Qiu, Y.; Lin, Y.; Yang, H. B.; Wang, L.; Wang, M. Q.; Wen, B. Hollow Ni/C microspheres derived from Ni-metal organic framework for electromagnetic wave absorption. *Chem. Eng. J.* **2020**, *383*, 123207.
[53] Kuchi, R.; Latif, T.; Lee, S. W.; Dongquoc, V.; Van, P. C.; Kim, D.; Jeong, J. R. Controlling the electric permittivity of honeycomb-like core–shell Ni/$CuSiO_3$ composite nanospheres to enhance microwave absorption properties. *RSC Adv.* **2020**, *10*, 1172–1180.
[54] Li, N.; Xie, X.; Lu, H. X.; Fan, B. B.; Wang, X. H.; Zhao, B.; Zhang, R.; Yang, R. Novel two-dimensional $Ti_3C_2T_x$/Ni-spheres hybrids with enhanced microwave absorption properties. *Ceram. Int.* **2019**, *45*, 22880–22888.
[55] Zheng, Y.; Zhang, W. D.; Zhang, X.; Zhu, Q.; Zhu, W. F.; Wang, R. M.; Qi, S. H. Structure and performance of Ni@Ni_3S_2 foam for microwave absorption. *J. Phys. D:Appl. Phys.* **2019**, *52*, 485003.
[56] Liu, D. W.; Du, Y. C.; Xu, P.; Liu, N.; Wang, Y. H.; Zhao, H. H.; Cui, L. R.; Han, X. J. Waxberry-like hierarchical Ni@C microspheres with high-performance microwave absorption. *J. Mater. Chem. C* **2019**, *7*, 5037–5046.
[57] Huang, L. N.; Chen, C. G.; Huang, X. Y.; Ruan, S. C.; Zeng, Y. J. Enhanced electromagnetic absorbing performance of MOF-derived Ni/NiO/Cu@C composites. *Compos. Part B:Eng.* **2019**, *164*, 583–589.
[58] Wang, Z. Z.; Yang, W.; Lv, Q. R.; Liu, S. Q.; Fang, Z. Ferromagnetic and excellent microwave absorbing properties of CoNi microspheres and heterogeneous Co/Ni nanocrystallines. *RSC Adv.* **2019**, *9*, 13365–13371.
[59] Gao, S. S.; An, Q. D.; Xiao, Z. Y.; Zhai, S. R.; Yang, D. J. Controllable N-doped carbonaceous composites with highly dispersed Ni nanoparticles for excellent microwave absorption. *ACS Appl. Nano Mater.* **2018**, *1*, 5895–5906.